Meas. Sci. Technol. **21** (2010) 075204 (8pp) doi:10.1088/0957-0233/21/7/075204

Transient sensing of liquid films in microfluidic channels with optofluidic microresonators

M Grad[1,4], C C Tsai[2], M Yu[3], D-L Kwong[3], C W Wong[2] and D Attinger[1]

[1] Laboratory for Microscale Transport Phenomena, Columbia University, New York, NY 10027, USA
[2] Optical Nanostructures Laboratory, Columbia University, New York, NY 10027, USA
[3] The Institute of Microelectronics, 11 Science Park Road, Singapore 117685, Singapore

E-mail: mg2705@columbia.edu

Received 14 January 2010, in final form 5 May 2010
Published 1 June 2010
Online at stacks.iop.org/MST/21/075204

Abstract
We demonstrate that optical ring resonators can be used as time-resolved refractive index sensors embedded in microfluidic channels. The nanophotonic structures are integrated into soft silicone microchannels interfaced with a transparent hard polymer manifold and standard microfluidic connections. The steady-state sensitivity, resolution and detection limit of the sensors are characterized using aqueous saline solutions at various concentrations. Time-resolved measurements are performed by sensing thin liquid films (0–400 nm) associated with oil/water segmented flow in microfluidic channels. The influence of the interrogation wavelength is investigated, and the optimal wavelength is determined. Millisecond resolution is demonstrated by sensing the shape of a single drop as it flows past the sensor. Finally, the film thickness between the droplet and the resonator is measured for different capillary numbers and channel diameters, and compared with existing theoretical and experimental results.

Keywords: optofluidic, microresonator, optical sensing, microfluidics, microchannels, film thickness, segmented flow

(Some figures in this article are in colour only in the electronic version)

1. Introduction

We describe the use of photonic micro-resonators as high-speed, label-free, integrated refractive index sensors in microfluidic devices. Recently, micro-ring [1–7], micro-racetrack [8] and photonic crystal [9, 10] resonators have been used as label-free biosensors for the detection of small quantities of biomolecules adsorbed on a surface [1, 4, 7–9], for the measurement of temperature and concentration of solutions [2, 3, 8, 9], and for optical trapping of particles [6]. Steady-state sensitivities, defined as the shift of resonant wavelength per refractive index $d\lambda/dn$, were reported in the range of 70–135 nm/refractive index unit (RIU) [2–4, 8, 9]. Detection limits, defined as the ratio of resolution to sensitivity, were reported between 10^{-5} and 10^{-7} RIU [3, 5, 8, 9]. Applications of micro-resonator sensors have mostly been to measure steady-state phenomena, such as concentrations or protein adsorption, or relatively slow transient measurements such as molecular binding reaction kinetics (time scale on the order of seconds or minutes) [4, 11].

In this paper, we use resonator sensors to study a recent, widely used development in microfluidics: the generation of a periodic pattern of immiscible plugs and slugs, called segmented flow, inside microchannels [12]. The flow recirculation associated with segmented flow enhances heat and mass transfer [13, 14] for lab-on-a-chip applications by several orders of magnitude. The thickness of the film between the plug and the solid wall plays an important role in the heat and mass transport [15]. For fully wetting systems, the film thickness depends on the channel size and shape,

[4] Author to whom any correspondence should be addressed.

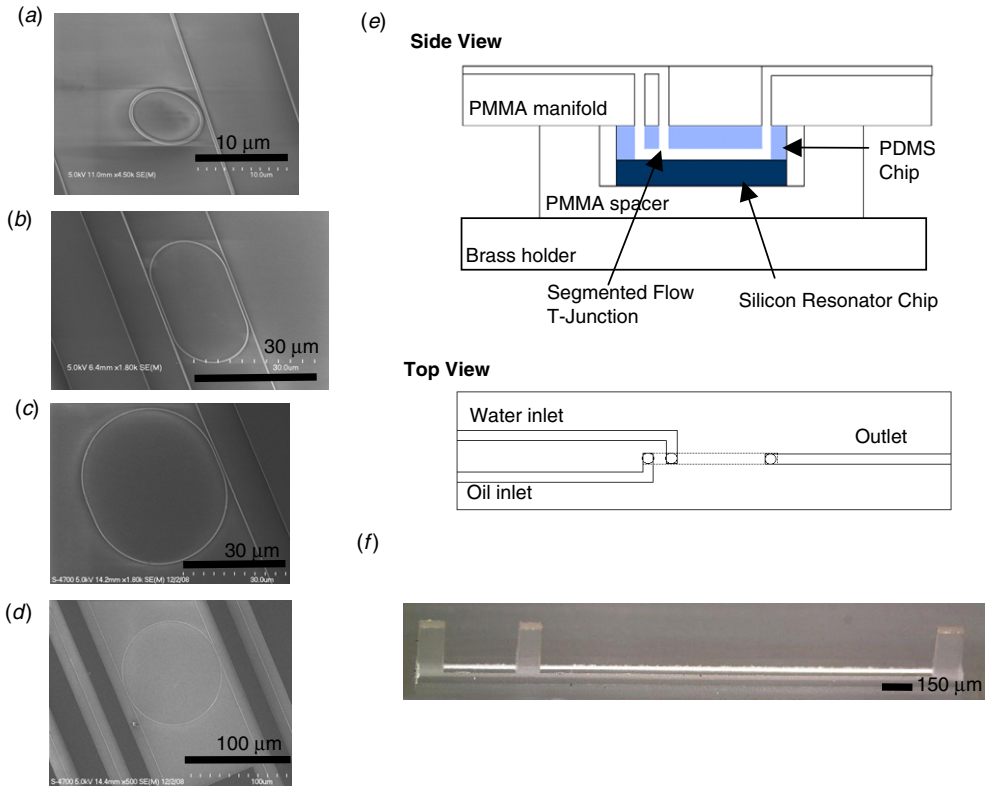

Figure 1. (*a*)–(*d*) Scanning electron microscope images of the micro-ring resonators. The waveguides are 250 nm high and 500 nm wide. (*a*) 8 μm two-port resonator. Full width half maximum ($\delta\lambda$) is 165 pm, and the Q-factor ($Q = \lambda_0/\delta\lambda$) is ∼9000. (*b*) 35 μm four-port resonator. $\delta\lambda$ is 140 pm, and the Q-factor is ∼11 000. (*c*) 45 μm two-port resonator. $\delta\lambda$ is 200 pm, and the Q-factor is ∼7500. (*d*) 106 μm four-port resonator. $\delta\lambda$ is 90 pm, and the Q-factor is ∼17 000. (*e*) Assembly of the sensor and microfluidic channel and connections. The channel is made from PDMS clamped between a PMMA manifold and the Si/SiO_2 substrate. (*f*) Mold used to fabricate the microchannel with three inlet and outlet pillars, machined into PMMA using a micromilling machine.

and on the ratio of the viscous forces over the capillary forces. That ratio is the capillary number ($Ca = \mu V/\gamma$), with V the slug velocity, μ the viscosity of the continuous phase and γ the surface tension between the two fluids. For cylindrical capillaries with diameter d, Bretherton formulated a theoretical law [16, 17] that predicts the film thickness $\delta \sim (d/2) \cdot Ca^{2/3}$. In square channels with height and width d, the film thickness in the middle of the wall with respect to the channel width is approximately constant at $(\delta/d)_{\text{const}}$, with most fluid filling the corners of the channel cross section [18], provided $Ca < Ca_{\text{trans}}$, a transition value. For $Ca > Ca_{\text{trans}}$, the film thickness increases and the plug tends to become axisymmetrical. The spatial constraints, transient flow conditions, and a high level of instrumentation of microfluidic chips make it challenging to integrate commercial thin film measurement instrumentation, such as optical interferometric profilers or ellipsometers. Consequently, the film thickness in microfluidic channels has been obtained through numerical simulation for square channels [15, 18] and measured with *ad hoc* optical setups for round capillaries [19–21] and square channels [22, 23]. The values of Ca_{trans} were 0.033 [18] and 0.025 [22], and values of $(\delta/d)_{\text{const}}$ were equal to 0.003 32 [18] and 0.0025 [22], respectively. In this paper, we investigate the use of fast, low-footprint, arrayable micro-resonator sensors for real-time measurements of liquid–liquid segmented flow in square channels.

2. Optical resonators

The optical racetrack resonators, shown in figure 1(*a*), consist of silicon waveguides ($n_{\text{Si}} = 3.4$) with thickness $t = 250$ nm, fabricated on top of a silica lower cladding layer ($n_{\text{SiO}_2} = 1.5$). The 500 nm wide waveguides are lithographically patterned with a 248 nm lithography scanner, and the Si is plasma etched. Four resonator sizes and shapes were tested, including an 8 μm two-port ring (figure 1(*a*)), a 35 μm four-port racetrack (figure 1(*b*)), a 45 μm two-port racetrack (figure 1(*c*)) and a 106 μm four-port ring (figure 1(*d*)). Light is confined within the waveguide due to total internal reflection at the interface between the silicon and its surrounding cladding layers. Perturbations in the refractive index of the upper cladding layer from different fluids in a microchannel (i.e. $n_{\text{water}} = 1.33$ and $n_{\text{oil}} = 1.43$) will cause changes in the effective index of refraction of the waveguides, altering the spectral location of their resonant peak. By measuring these resonance shifts we exploit these resonators as refractive index sensors.

Light from a continuous-wave tunable laser source (HP-8168F, 1 pm resolution) was coupled to the waveguides by a lensed optical fiber with a ∼2 μm Gaussian waist by *xyz*-nanopositioners with a 20 nm spatial resolution. The output light was led along a similar optical fiber into a high speed InGaAs photodetector (Thorlabs DET10C, 10 ns rise time).

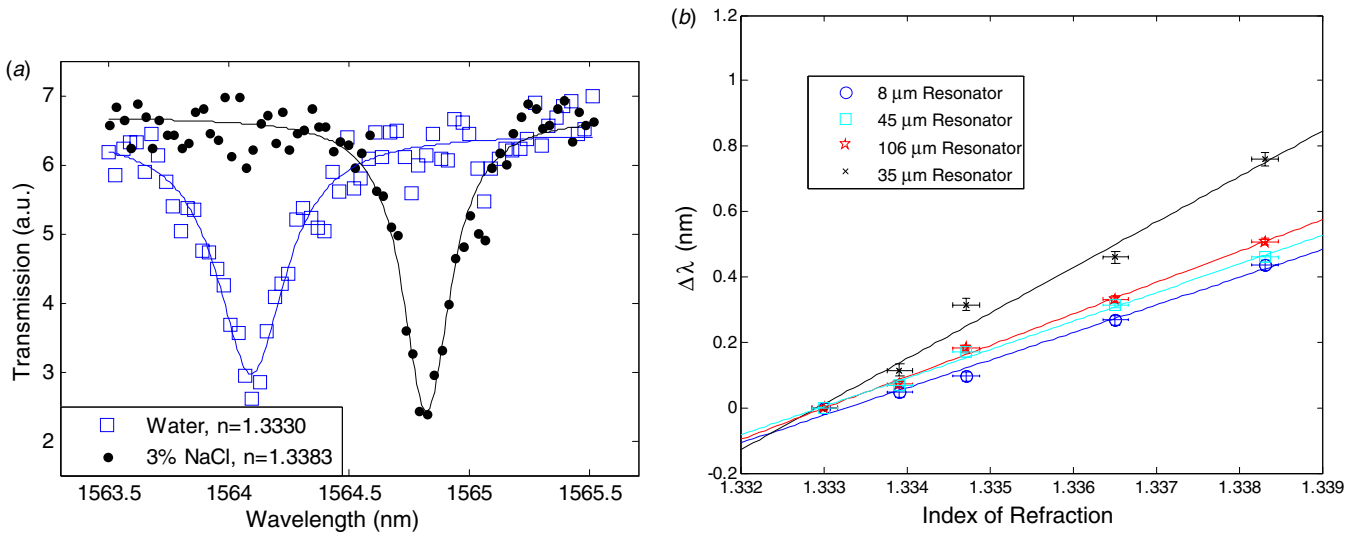

Figure 2. (*a*) Example of steady-state resonance shifts from different concentrations of salt solutions flowed along the microchannel. Lorentzian curves are fitted to the resonant peaks. (*b*) Measured resonance shifts as a function of the salt concentration, with linear regression.

Steady-state measurements were performed by scanning the laser through a narrow frequency band. A lock-in amplifier (Stanford Research, SR510) was used to locate the resonant peak, λ_0, with the help of a Lorentzian curve fit. Time-resolved measurements were performed by choosing a single wavelength (i.e. the resonant wavelength with oil on the surface) and recording the signal change as the resonant peak shifted past that wavelength. A transimpedance amplifier (Melles Griot, USA) was used to transform the current coming from the photodetector into the output voltages that will be discussed in section 4.

3. Manufacturing and integration

The microfluidic channels are cast in the soft silicone rubber polydimethylsiloxane (PDMS, Dow Corning) using a mold machined into polymethylmethacrylate (PMMA) by a computer numerically controlled (CNC) micromilling machine (Minimill 3, Minitech Machinery). The accuracy of the milling machine is 2–5 μm, with a surface roughness below 100 nm. A sample mold is shown in figure 1(*f*), and consists of a 150 μm channel with three pillars. The advantages of using a micromilling machine over typical SU-8 lithographic methods are shorter manufacturing times and a wider choice of design shapes: high aspect ratios and non-planar surfaces can be easily machined (i.e. the pillars) and a clean room is not required. Also the scale of the micromilling machine abilities (μm–mm) is ideal for multiphase microfluidics because it bridges the gap between lithography (nm–μm) and conventional milling (mm–m).

The PDMS was poured and cured over the master to the height of inlet and outlet pillars, creating through-holes. A manifold was machined out of PMMA to the interface between the through-holes and standard microfluidic connections (Upchurch Scientific, USA). The bottom of the PDMS channel was aligned directly onto the Si/SiO_2 sensor chip and clamped between the manifold and the substrate by four screws. A spacer was machined at the proper height to ensure that the PDMS chip was not overclamped. Figure 1(*e*) shows a schematic of the fluidic assembly.

4. Experimental results

4.1. Steady state measurements

The four resonators were first tested by flowing aqueous solutions with different concentrations of dissolved NaCl salt in the microchannel, corresponding to refractive indices between 1.3330 and 1.3383 [24]. Figure 2(*a*) shows a typical shift in resonance resulting from a change in concentration from pure water to 3% saline solution for the 35 μm resonator. Lorentzian curves are fitted to the experimental data points in the graph, i.e.

$$y - y_0 = \frac{2A}{\pi}\left[\frac{W}{4(\lambda - \lambda_0)^2 + W^2}\right], \qquad (1)$$

where y is the output voltage, y_0 is an offset value, A is a voltage amplitude, W is the width of the peak at half the maximum value (FWHM) and λ_0 is the resonant wavelength. Figure 2(*b*) plots the linear shifts $\Delta\lambda$ as a function of the NaCl concentration, with the center of the resonance peak determined from the Lorentzian least squares curve fit, for the four resonators that we have tested. Each data point was averaged from three scans around the resonant peak, with vertical error bars expressing the standard deviation, and horizontal error bars expressing the uncertainty in temperature that results in uncertainty in the refractive index.

The quality factors (Q-factors) of the resonators, defined as $\lambda_0/\delta\lambda$ where $\delta\lambda$ is the full width at half the maximum amplitude and λ_0 is the resonant wavelength, were calculated to range from 7500 to 17 000. The steady-state sensitivities of the resonators, defined as $d\lambda/dn$ [5] with units nm RIU^{-1}, ranged from approximately 84 to 139 nm RIU^{-1}. The

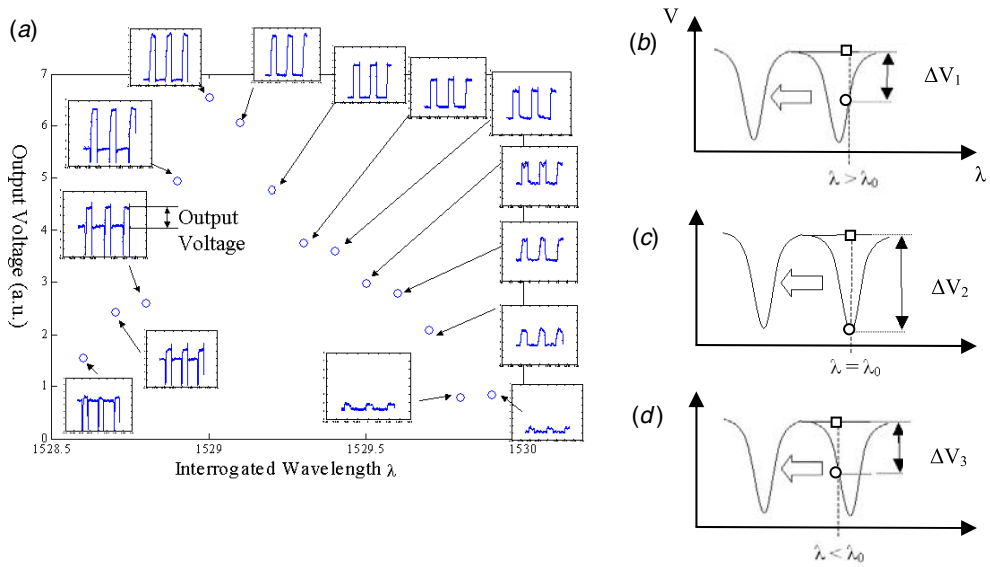

Figure 3. (*a*) Example output voltages from the sensor in 100 μm channels for different interrogated wavelengths, with $Ca = 0.002$. The axes on the inset graphs are time and voltage. The output voltage is the difference between the low and high voltage plateaus, corresponding respectively to oil slugs or water plugs flowing over the sensor. The sharp decreases are ignored. (*b*)–(*d*) Phenomenological graphs explaining a sharp decrease in voltage before and after a plug flows over the resonator, as seen in the insets of figure 2(*a*). The circles represent the signal from the photodetector when the sensor is covered with oil, and the squares represent the signal from the photodetector when the sensor is covered with a water droplet and thin oil film. The output voltage is the difference between these two values.

resolution of these resonators is defined as 3σ of the noise in the system, where the noise consists of amplitude noise, thermal fluctuations and spectral resolution [5]. The amplitude noise is related to the quality factor of the resonator, and is estimated numerically from Monte Carlo simulations in [5] to range from: $\sigma_{\text{amplitude}} = \frac{\delta\lambda}{4.5(\text{SNR}^{0.25})} \approx 2$–$4.4$ pm, where $\delta\lambda$ is the full width at half the maximum value (ranging from 90 to 140 pm) and SNR is the signal to noise ratio in linear units ($\sim 10^4$). The spectral resolution of the laser is 1 pm and has a standard deviation of 0.29 pm. Thermal noise is caused by $\sim 3^\circ$ fluctuations in the ambient temperature, resulting in $\pm 1 \times 10^{-4}$ RIU, or ± 1.4 pm shifts. Therefore, the total resolutions range from approximately 3.4 to 5.8 pm. The detection limit is the ratio of resolution to sensitivity, $\text{DL} = R/\text{S}$, and ranges for these resonators from 3.23×10^{-5} to 6.9×10^{-5} RIU [5]. The 35 μm four-port resonator was determined to have the lowest detection limit and was therefore used in the subsequent time-resolved experiments.

4.2. Time-resolved measurements: interrogation wavelength

To perform time-resolved measurements, we first studied the effects of the selection of a proper interrogation wavelength. For a given flow rate, the interrogated wavelength was scanned around a resonant peak as trains of droplets flowed over the sensor. Figure 3(*a*) shows the output voltages for segmented flow in a 100 μm channel. The capillary number was calculated to be 0.002, which, from correlated experimental and numerical studies [18, 22], corresponds to an estimated oil film thickness of between 250 and 300 nm.

The transient voltage inserts in figure 3(*a*) can be explained using the phenomenological figures on the right, for three different interrogation wavelengths. When oil is on top of the resonator, the circles shown in figures 3(*b*)–(*d*) represent the voltage from the photodetector. When a water droplet and its thin oil film are on top of the resonator, the voltage from the photodetector assumes the value represented by the squares in figures 3(*b*)–(*d*), because the reduced effective index of refraction shifts the resonant peak to the left. When the interrogated wavelength is higher than the resonant wavelength, as in figure 3(*b*), the voltage jumps by ΔV_1. When the interrogated wavelength is equal to the resonant wavelength, as in figure 3(*c*), the voltage jumps by ΔV_2. Finally, when the interrogated wavelength is less than the resonant wavelength as in figure 3(*d*), the voltage first decreases as the resonant peak shifts past the interrogated wavelength and then increases by ΔV_3. Therefore, the left side of the figure shows sharp decreases in output voltage before and after the droplet passes. The output voltage is defined by the difference between the low and high voltage plateaus, ignoring these sharp decreases. Figure 3(*a*) shows that there is a maximum signal that can come from a chosen interrogation wavelength. For the rest of the measurements in this paper, a narrow scan was performed to ensure that the signal is at a maximum (i.e. $\lambda = \lambda_0$) before taking measurements at $\lambda = \lambda_0$.

4.3. Time-resolved measurements: temporal resolution

The time resolution of the sensing is demonstrated by measuring the shape of a droplet. Figure 4(*a*) shows the voltage from an overall train of small droplets ($L_{\text{drop}} \sim 200$ μm). As confirmed in figure 4(*b*), a droplet flowing in a microchannel is typically bullet-shaped, which means that a fixed sensor measuring film thickness would measure a transition from the oil slug to the film slower for the front of the drop than for its rear. Fourteen sets of voltage measurements

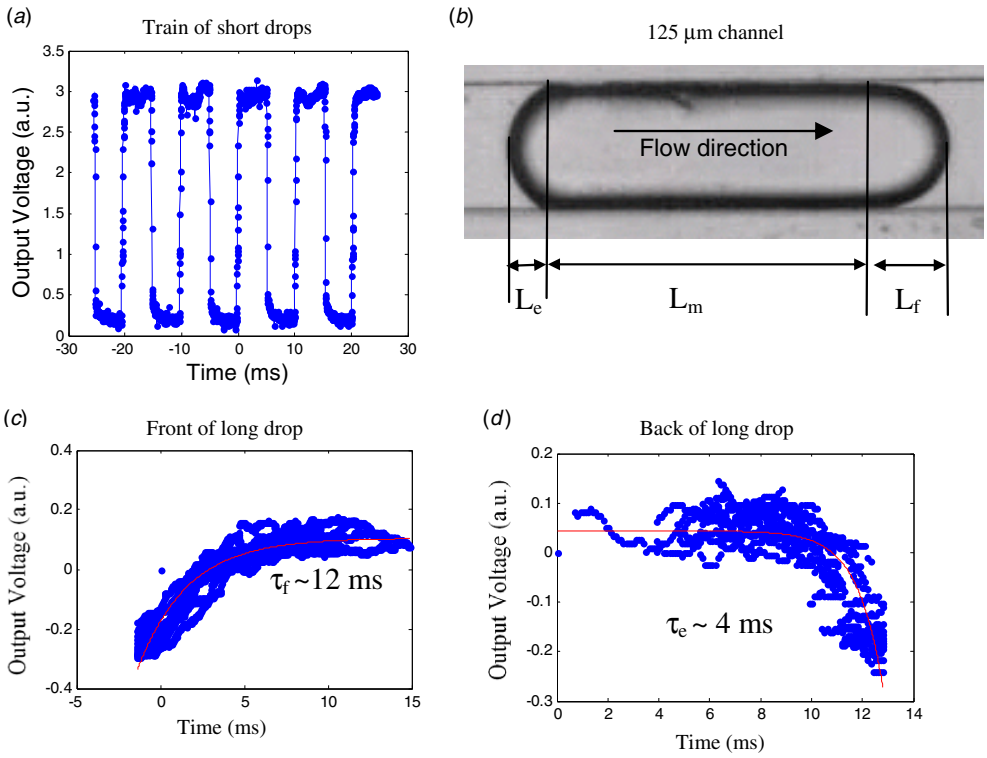

Figure 4. (*a*) Voltage from a train of short drops passing over the sensor, with $L_{\text{total}} \sim 200\ \mu$m. (*b*) Photograph of a drop flowing with $Ca = 0.002$ along a 125 μm channel, showing lengths L_f, L_m and L_e. The ratio L_f/L_e corresponds to the ratio τ_f/τ_e because the plug velocity is constant. Finally, voltages measured during the transit of the (*c*) front, (*d*) rear sections of a longer drop passing over the sensor, with $L_{\text{total}} \sim 2$ mm. Fourteen sets of voltage measurements are split into sections, normalized by subtracting their mean value and plotted simultaneously. Exponential curves are then fitted to the front and rear ends of the drop, to identify time constants τ_f and τ_e.

were then taken for individual drops passing over the sensor and analyzed in three sections, corresponding to the front, middle and end of the drop, and figures 4(*c*), (*d*) show the voltages from the front and rear sections of longer droplets ($L_{\text{drop}} \sim 2$ mm). It is important to note that the noise in figures 4(*c*), (*d*) probably comes from the slight variation in droplet volume or shape between drops. The curve fits in figures 4(*c*) and (*d*) show that the time scale of the film thickness change is about three times slower at the front of the drop (τ_f) than at the end of the drop (τ_e). Since the plug is moving at a constant velocity, the ratio of radii of curvature of the front and end sections L_f/L_e should be proportional to the ratio of time constants τ_f/τ_e. Figure 4(*b*) shows that L_f/L_e is approximately 2.5 and is in agreement with τ_f/τ_e. These measurements demonstrate that the ring resonator measurements can resolve transient time scales on the order of a few milliseconds.

4.4. Time-resolved measurements: film thickness in segmented flow

The micro-ring resonator sensors were used to measure the film thickness associated with oil/water segmented flow, an important parameter governing the heat and mass transfer to the wall [15]. The film thickness above the resonator was varied in two ways: first by changing the flow rate in a single channel to increase the capillary number, and then by changing the channel diameters and keeping $Ca < Ca_{\text{trans}}$. The signal from our resonator is shown for these cases in figures 5(*a*) and (*b*), respectively. In figure 5(*a*), the channel size is 125 μm and the capillary number was varied from 0.001 to 0.1. In figure 5(*b*), the capillary number was maintained at 0.002 and the square channel cross sections were varied from 100 to 200 μm. The trends of film thickness with respect to the channel size and capillary number are then compared to previously published values of air/water segmented flow.

In our measurements, the sensor's signal was converted to film thickness in the following manner. First, we measured the transmission as a function of the wavelength for a resonator submerged in pure water (figure 2(*a*)). Then we measured the transient output voltages described in section 4.2 for the system experiencing oil/water segmented flow. These output voltages are the transmission changes on the vertical axis of figure 2(*a*), and corresponding shifts in the resonant wavelength $\Delta\lambda$ are obtained from the horizontal axis of this figure. This is mathematically expressed by rearranging the equation for the Lorentzian curve fitted to the data, discussed in section 4.1, where y_0 and λ_0 are the unperturbed (i.e. when oil covers the sensor) output voltage and resonant wavelength, and are determined from experiments and the Lorentzian curve fits. Then the first-order perturbation Δn_{eff} of the effective index is obtained from $\Delta\lambda$ by [25]

$$\frac{\Delta n_{\text{eff}}}{n_{\text{eff}\,0}} = \xi \frac{\Delta\lambda}{\lambda_0}, \tag{2}$$

where ξ is the fraction of the mode exposed outside of the waveguide. The value for ξ is typically ~0.5 [25],

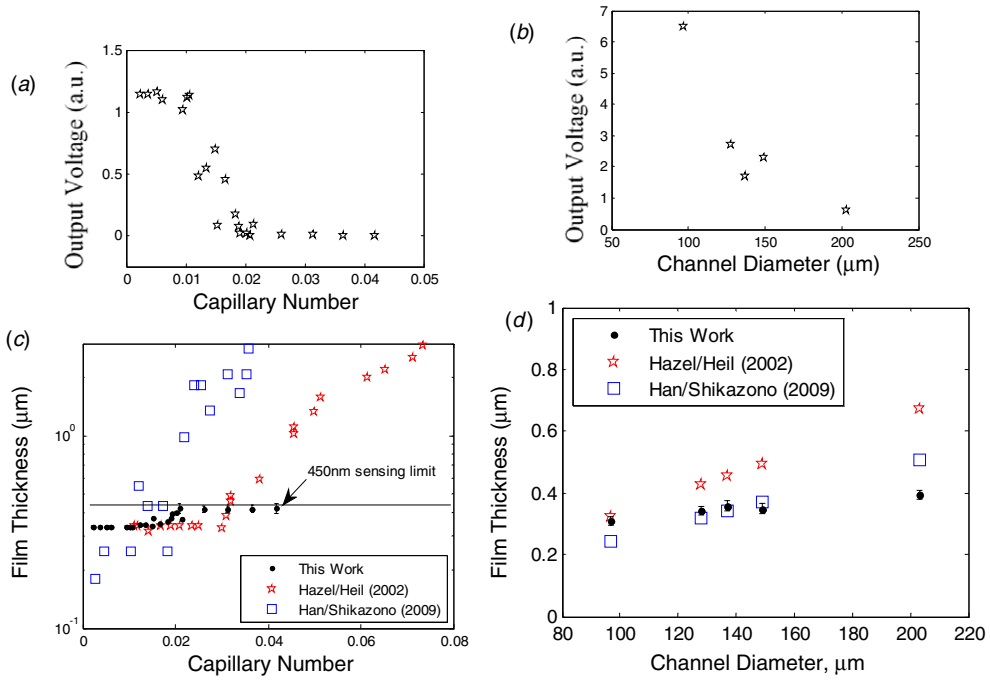

Figure 5. (*a*) Output voltage as a function of the capillary number for a constant channel width of 125 μm. (*b*) Output voltage as a function of the channel width, for $Ca = 0.002$ (*c*) Film thickness measured from output voltages as a function of the capillary number for constant channel width. Also plotted on the same graph are numerical simulations from Hazel and Heil [18] and experimental results from Han and Shikazono [22]. (*d*) Film thickness measured from output voltages as a function of the channel width for the constant capillary number. Also plotted on the same graph are numerical simulations from Hazel and Heil [18] and experimental results from Han and Shikazono [22]. The error bars are calculated by the propagation of a 0.1 V output voltage uncertainty through the film thickness calculation.

but was measured here from steady-state experiments with aqueous salt solutions in figure 2(*b*) to be equal to 0.21. In equation (2), $n_{\mathrm{eff},0}$ is the unperturbed (i.e. only oil covering the sensor) effective index of refraction, determined from *Rsoft* BeamProp simulations.

To numerically calculate the effective index of refraction of the waveguide, it is important to know the shape assumed by the film while flowing over the waveguide. Blyth and Pozrikidis [26] performed numerical simulation of the film deformation over a hemispherical obstacle, assuming negligible inertia. Their results show a hump slightly upstream of the obstacle and a horseshoe-shaped deformation downstream, and were also confirmed in [27]. Our experiments exhibit average film velocities ranging from 0.01 m s^{-1} to 0.1 m s^{-1} and Reynolds numbers below 0.1, and therefore fall in the Stokes flow regime assumed in [26]. The film deformation corresponding to the simulations in [26] was used in our 2D numerical simulations of effective index of refraction. The simulation results shown in figure 6 relate the effective index of refraction n_{eff} to the film thickness. The maximum change in refractive index occurs for films thinner than ~450 nm. For films thicker than that value, the resonant peak is not expected to shift, and films thinner than 250 nm were not included because they are smaller than the waveguides. This important limitation of our sensor arises because the resonators are only sensitive to changes in refractive index in their immediate vicinity, since the confined light decreases exponentially away from the waveguide. The equation fit to these simulations is

$$\delta = \delta_0 + B(n_{\mathrm{eff}} - n_{\mathrm{eff},0})^k, \tag{3}$$

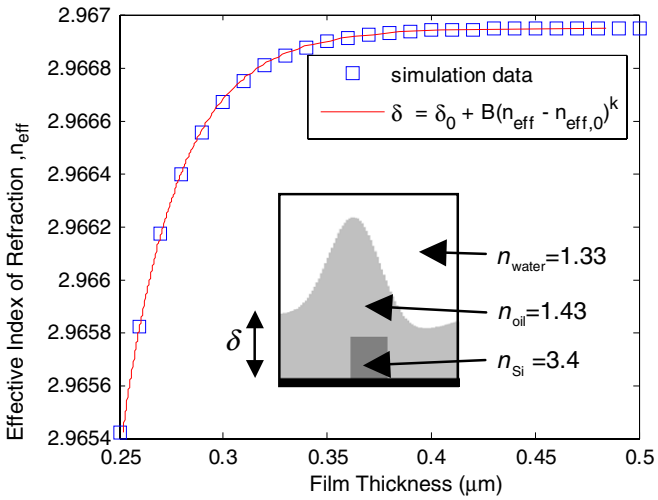

Figure 6. Simulations of the effective index of refraction as a function of the film thickness, and curve fitted to the simulation data. Inset: simulation geometry, with the wavy oil–water interface obtained from simulations in [26].

where A_1 and k are the fitting parameters found to be approximately 0.86 and 0.027, respectively. It is possible to combine equations (1)–(3) to relate the output voltage to film thickness:

$$\delta - \delta_0 = B\left(\frac{\xi \cdot n_{\mathrm{eff}\ 0}}{2\lambda_0}\right)^k \left[\frac{2AW}{\pi\,(y - y_0)} - W^2\right]^{\frac{k}{2}}, \tag{4}$$

where B, ξ, $n_{\text{eff},0}$, λ_0, k, A and W are constants defined in the previous equations. This overall equation relates the perturbations in film thickness to the changes in output voltage. It is important to note that due to the simulations and fitting parameters, these equations only apply to the geometry of our system.

The values of film thickness measured with our sensors are shown as a function of the capillary number in figure 5(*c*). The error bars were calculated by the propagation of a 0.01 V output voltage uncertainty through equation (4), and the maximum film thickness uncertainty is approximately 15 nm. The film thickness uncertainty is larger when the voltage difference is near zero; therefore, the error bars are only visible at larger capillary numbers where the voltage differences are small. At low capillary numbers ($Ca < 0.01$) our measurements show that the film thickness is constant and approximately equal to the value found by Hazel and Heil [18], ~330 nm for the 100 μm channel. At capillary numbers greater than ~0.03, the sensor reaches its limit of film thickness detection of ~450 nm. The transition capillary number between constant film thickness and increasing film thickness occurs at around $Ca_{\text{trans}} \sim 0.01$, as shown by the increase in film thickness. Our measurements show that this transition point occurs at slightly lower Ca values than the reported experiments by Han and Shikazono ($Ca_{\text{trans}} \sim 0.025$) for air/water segmented flow [22], and the numerical simulation by Hazel and Heil ($Ca_{\text{trans}} \sim 0.033$) [18], which are both plotted on the same graph. This discrepancy between our results and the previously published results may be caused by the difference in the sensing range and resolution of the measurement methods, or by the difference between air/water and oil/water segmented flows. But to the best of the author's knowledge, film thickness measurements for oil/water segmented flow in square channels have not been published. In any case, the shape of both our and the previously published curves is the same until the limit of our sensor is reached.

The sensor results of film thickness as a function of the channel width are shown in figure 5(*d*). For comparison, the graph also includes the numerical simulations of film thickness from Hazel and Heil [18] and the optical measurements from Han and Shikazono [22]. All three sets of data show similar orders of magnitude and display the trend that film thickness increases as the channel width increases.

5. Conclusion

We have shown that optical resonators can be used as high-speed refractive index sensors embedded in microfluidic channels. The nanophotonic structures range from 8 to 106 μm in size, are arrayable and are sensitive to changes to the index of refraction of the fluids passing over them. Their sensitivity, resolution and detection limit were investigated at steady state using different concentrations of NaCl. These structures were then used for the high-speed sensing of film thickness associated with segmented flow. First, the interrogation wavelength was optimized for the rest of the experiments. Next, the shape of a single drop was investigated to demonstrate temporal resolution. Finally, the film thickness was investigated by individually varying the capillary number and the channel diameter, and found in qualitative and quantitative agreement with previous theories and experiments.

Acknowledgments

The authors acknowledge discussions with A R Betz, J Xu, S Kocaman and J F McMillan, and funding support from NSF grant 0701729 and the Mechanical Engineering Department at Columbia University.

References

[1] Ksendzov A and Lin Y 2005 Integrated optics ring-resonator sensors for protein detection *Opt. Lett.* **30** 3344–6
[2] Kwon M S and Steier W H 2008 Microring-resonator-based sensor measuring both the concentration and temperature of a solution *Opt. Express* **16** 9372–7
[3] Chao C Y, Fung W and Guo L J 2006 Polymer microring resonators for biochemical sensing applications *IEEE J. Sel. Top. Quantum Electron.* **12** 134–42
[4] Yalçin A *et al* 2006 Optical sensing of biomolecules using microring resonators *IEEE J. Sel. Top. Quantum Electron.* **12** 148–54
[5] White I M and Fan X 2008 On the performance quantification of resonant refractive index sensors *Opt. Express* **16** 1020–8
[6] Lin S and Crozier K 2009 Optical trapping using planar silicon micro-ring resonators *Frontiers in Optics* OSA Technical Digest (CD) (Optical Society of America) paper PDPC8
[7] Vollmer F and Arnold S 2008 Whispering-gallery-mode biosensing: label-free detection down to single molecules *Nat. Methods* **5** 591–6
[8] De Vos K, Bartolozzi I, Schacht E, Bienstman P and Baets R 2007 Silicon-on-Insulator microring resonator for sensitive and label-free biosensing *Opt. Express* **15** 7610–5
[9] Mandal S and Erickson D 2008 Nanoscale optofluidic sensor arrays *Opt. Express* **16** 1623–31
[10] Smith C L C *et al* 2008 Reconfigurable microfluidic photonic crystal slab cavities *Opt. Express* **16** 15887–96
[11] Fan X, White I M, Shopova S I, Zhu H, Suter J D and Sun Y 2008 Sensitive optical biosensors for unlabeled targets: a review *Anal. Chim. Acta* **620** 8–26
[12] Thorsen T, Roberts R W, Arnold F H and Quake S R 2001 Dynamic pattern formation in a vesicle-generating microfluidic device *Phys. Rev. Lett.* **86** 4163–6
[13] Betz A R and Attinger D 2010 Can segmented flow enhance heat transfer in microchannel heat sinks? *Int. J. Heat Mass Transfer* at press, doi:10.1016/ijheatmasstransfer.2010.04.016
[14] Burns J R and Ramshaw C 2002 A microreactor for the nitration of benzene and toluene *Chem. Eng. Commun.* **189** 1611–28
[15] Kreutzer M T, Kapteijn F, Moulijn J A and Heiszwolf J J 2005 Multiphase monolith reactors: chemical reaction engineering of segmented flow in microchannels *Chem. Eng. Sci.* **60** 5895–916
[16] De Gennes P-G 2004 *Capillarity and Wetting Phenomena: Drops, Bubbles, Pearls, Waves* (New York: Springer Science)
[17] Bretherton F P 1961 The motion of long bubbles in tubes *J. Fluid Mech. Digit. Arch.* **10** 166–88

[18] Hazel A L and Heil M 2002 The steady propagation of a semi-infinite bubble into a tube of elliptical or rectangular cross-section *J. Fluid Mech.* **470** 91–114
[19] Ji H F and Qiu H H 2009 2D fringe probing of liquid film dynamics of a plug bubble in a micropipe *Meas. Sci. Technol.* **20** 025402
[20] Kraus T, Gunther A, De Mas N, Schmidt M A and Jensen K F 2004 An integrated multiphase flow sensor for microchannels *Exp. Fluids* **36** 819–32
[21] Qiu H, Wang X and Hong F 2005 Measurements of interfacial film thickness for immiscible liquid-liquid slug/droplet flows *Meas. Sci. Technol.* **16** 1374–80
[22] Han Y and Shikazono N 2009 Measurement of liquid film thickness in micro square channel *Int. J. Multiphase Flow* **35** 896–903
[23] Kolb W B and Cerro R L 1991 Coating the inside of a capillary of square cross section *Chem. Eng. Sci.* **46** 2181–95
[24] Lide D (ed) 2006 *CRC Handbook of Chemistry and Physics* vol 86 (Boca Raton, FL: Taylor and Francis)
[25] Johnson S G, Ibanescu M, Skorobogatiy M A, Weisberg O, Joannopoulos J D and Fink Y 2002 Perturbation theory for Maxwell's equations with shifting material boundaries *Phys. Rev.* E **65** 066611
[26] Blyth M G and Pozrikidis C 2006 Film flow down an inclined plane over a three-dimensional obstacle *Phys. Fluids* **18** 052104
[27] Baxter S J, Power H, Cliffe K A and Hibberd S 2009 Three-dimensional thin film flow over and around an obstacle on an inclined plane *Phys. Fluids* **21** 032102